UC Davis
UC Davis Previously Published Works

Title
On the effect of cold-rolling on the corrosion of SS316L alloy in a molten carbonate salt

Permalink
https://escholarship.org/uc/item/1vs6h9dr

Authors
Sarvghad, Madjid
Muránsky, Ondrej
Steinberg, Theodore A
et al.

Publication Date
2019-11-01

DOI
10.1016/j.solmat.2019.110136

Peer reviewed

On the effect of cold-rolling on the corrosion of SS316L alloy in a molten carbonate salt

Madjid Sarvghad[1*], Ondrej Muránsky[2,3], Theodore A. Steinberg[1], James Hester[2], Michael R. Hill[4], Geoffrey Will[1]

[1] Science and Engineering Faculty, Queensland University of Technology (QUT), Queensland, Australia

[2] Australian Nuclear Science and Technology Organization (ANSTO), New Illawarra Road, Lucas Heights, NSW, Australia
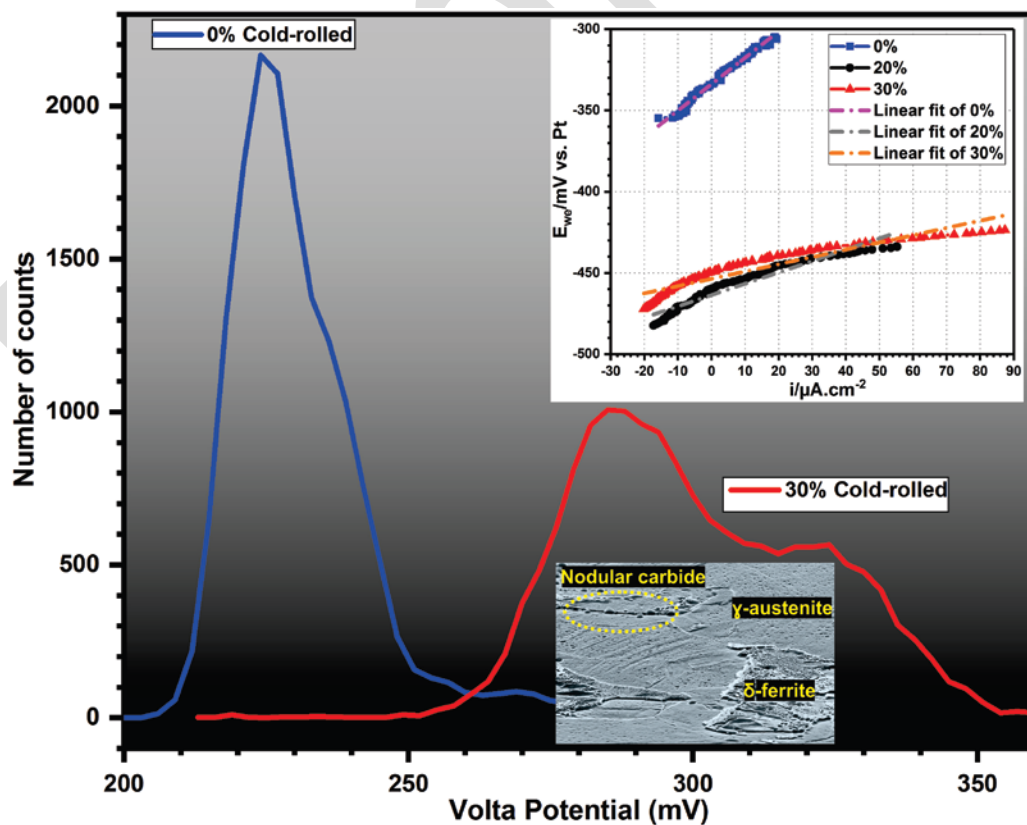
[3] School of Materials Science and Engineering, University of New South Wales (UNSW), Sydney, Australia

[4] Mechanical and Aerospace Engineering Department, University of California, Davis, USA

[*] Corresponding author; Email: Sarvghad_madjid@hotmail.com; madjid.sarvghadmoghaddam@hdr.qut.edu.au

1

Abstract

Interactions between stainless steel 316L and eutectic $Li_2CO_3 + K_2CO_3 + Na_2CO_3$ at 450 ˚C were investigated for thermal energy storage. Scanning Electron Microscopy (SEM), Electron Back-Scatter Diffraction (EBSD), Scanning Kelvin Probe Force Microscopy (SKPFM), X-ray Photoelectron Spectroscopy (XPS), neutron diffraction pattern, material loss, micro-hardness, polarization and impedance measurements were used to compare the alloy's response in unrolled (0%) condition versus 20% and 30% cold-rolled conditions. Cold-rolling increased the number of grains, grain boundaries and density of dislocations. Initially, faster corrosion accompanied by more areas of localized attack was confirmed by Volta potential measurements. However, recovery and the formation of a surface film were found to decelerate corrosion for longer times. Cold-rolling-induced dislocations were found to facilitate carbon diffusion and subsequently carburize the material leading to increased corrosion resistance. Consequently, the overall long-time corrosion rate was not noticeably affected by cold-rolling.

Keywords

Stainless steel; Molten salt; Electrochemical calculation; Diffraction pattern; High temperature corrosion; Carburization

1. Introduction

Stainless Steel alloys are commercially well-known as affordable construction materials for high-temperature applications as they typically maintain high strength and corrosion (oxidation) resistance at elevated temperatures [1-3]. Hence, stainless steel alloys are currently being considered as structural materials for application in Concentrated Solar Power (CSP) and Thermal Energy Storage (TES) systems [4, 5]. These advanced energy-generation and energy-storage systems use Phase Change Materials (PCMs), typically eutectic compositions of molten salts, to act as both energy-transfer and energy-storage media [6-10]. The operating temperature of the system is usually close to (or just above) the melting point of the PCM. The utilized structural materials need to withstand challenging operation conditions of high temperature, molten salt (PCM) corrosion and thermal cycling around the melting point of the salt. The combination of high-temperature creep, thermal-fatigue and molten-salt corrosion lead to severe material degradation during operation, significantly affecting the expected lifetime of a component in service and the economies of the system [11]. It is therefore technologically important to understand and predict the degradation mechanisms of structural materials under typical operational conditions.

It is a common practice to improve the material properties of the already well-established materials (e.g. SS316, SS304, or Inconel 690, etc.) by additional processing (e.g. cold-rolling, laser peening, shot peening, etc.) [12, 13]. This is considered a more cost-effective approach than development of new alloys, which would then require costly standardization and industrial acceptance. Cold-rolling is a simple and effective process that can be performed on ductile alloys in order to increase their yield and tensile strength [14]. Cold-rolling dramatically increases the number of crystal lattice defects (dislocations, shear bands, as well as low- and high- angle grain boundaries) which provide significant work-hardening and an associated increase in the strength of the material. However, it has been shown that the presence of crystal lattice defects can negatively affect the material behavior in service [15-20]. For instance, a number of recent studies have shown that cold-rolling decreases the material resistance to Stress Corrosion Cracking (SCC) [21, 22], which is of utmost importance in CSP and nuclear reactors. This is thought to occur because of the aforementioned crystal lattice defects introduced to the microstructure during the cold-rolling process providing a preferential pathway for atomic/molecular

3

diffusion [23]. The introduction of both macroscopic and microscopic stresses into the surface of the material during plastic deformation could further exacerbate the material susceptibility to SCC [23, 24]. It has been further shown that, by using the Scanning Kelvin Probe Force Microscopy (SKPFM) technique, a correlation exists between the electrochemical behavior of Inconel 601 alloy and the density of lattice defects [20]. Similarly, Raabe [25] has shown that the high densities of lattice defects can alter the electro-chemical potential around defects and thus change the electrical resistivity of the material, which will subsequently affect its corrosion behavior.

This study investigates the effect of cold-rolling on the corrosion behavior of SS316L stainless steel alloy in the eutectic mixture of Li_2CO_3 + K_2CO_3 + Na_2CO_3 (molten salt) at 450 ˚C. This is a promising PCM for CSP applications in moderate temperature (<500 ˚C) TES systems because of its high thermal stability (up to around 1000 ˚C under CO_2 atmosphere and 600 ˚C in air) and latent heat capacity (276 kJ.kg^{-1}) [8, 26-28]. The SS316L alloy was tested in three cold-rolled conditions: unrolled (0%), 20%, 30% cold-rolled. First, the impact of cold-rolling on the microstructure was examined using microscopy and diffraction techniques. Second, the corrosion behaviors of unrolled (0%) and cold-rolled (20%, 30%) samples were evaluated using static corrosion, electrochemical and Volta potential measurements. Further analysis was performed using hardness measurement and X-ray spectroscopy techniques. A correlation between the amount of cold-rolling, microstructure and corrosion behavior was then established based on the experimental data.

2. Experimental

2.1. Material and samples

Testing was conducted on a set of SS316L plates, all cut from a single heat (610344-3A) obtained from American Stainless Corporation. The chemical composition is given in Table 1. SS316L alloy is austenitic (γ-austenite, FCC) at room temperature, although a small amount of δ-ferrite (BCC) is present, allowing for easier hot machinability by providing resistance to cracking at elevated temperatures. Based on the Schaeffler diagram, performed neutron diffraction (described below) and microstructural examination it was confirmed that there is about 5% of δ-ferrite present in the microstructure of the used SS316L alloy.

4

Two hot-rolled, annealed and pickled per ASME SA-240 316L plates, each 127 (x) × 355.6 (z) × 25.4 (y) mm (Fig. 1), were unidirectionally cold-rolled to levels of 20% and 30% thickness reduction. A third plate of the same material and dimensions did not undergo deformation, and is referred to as the 0% (unrolled) condition. The final thicknesses (t) of the prepared SS316L plates are presented in Table 2 alongside the obtained mechanical properties (yield strength, ultimate tensile strength and total elongation). Mechanical testing was done at the University of California, Davis (USA).

Table 1 Chemical composition of SS316L plates (wt.%) obtained from material certification by American Stainless Corporation.

Fe	C	Cr	Ni	Mo	Mn	Cu	Si	Co	P	S
Bal	0.019	16.46	10.07	2.04	1.59	0.39	0.35	0.32	0.033	0.011

Table 2 Mechanical properties of the studied SS316L plates.

Thickness reduction [%]	Plate thickness (t) [mm]	Yield strength [MPa]	Ultimate tensile strength [MPa]	Total elongation [%]
0%	25.4	347	602	54
20%	20.32	723	863	34
30%	17.78	821	957	31

Samples for microstructural investigation and molten salt testing were extracted from each plate using wire Electric Discharge Machining (EDM) so that only half of the plate was used for the experimental work as shown in Fig. 1; symmetry along the plate mid-plane (y/2) was checked. Plate-like samples of different dimensions were prepared for static corrosion and electrochemistry as shown in Fig. 1. In addition, a cylinder with a diameter of 5 mm and length of y/2 was extracted from each plate using EDM for neutron diffraction measurements.

Where necessary (noted in the following sections), samples were mechanically wet ground and polished down to 0.04 µm with colloidal silica (using standard EBSD procedure [29]), washed with ethanol and dried with compressed air.

2.2. Microstructure

The effect of cold-rolling on the microstructure of SS316L alloy was studied using Electron Back-Scatter Diffraction (EBSD) and High-Resolution Neutron Diffraction (HRND). EBSD provides high spatial resolution information about the microstructure by sampling hundreds of grains in a single 300×300 µm^2 map while the HRND provides bulk-information averaging thousands of grains within the volume of the sample (cylinder: 5 mm in diameter, y/2 mm in length, Fig. 1).

2.2.1. Electron Back-Scatter Diffraction (EBSD)

Multiple (up to 12) EBSD orientation maps were collected on every cold-rolled sample condition (as-polished) in order to obtain statistically significant grain statistics to determine bulk (microstructure-averaged) characteristics. A Zeiss® UltraPlus™ scanning electron microscope (SEM) equipped with an Oxford Instruments® AZtec™ EBSD system and a Nordlys-S™ EBSD detector was used for collecting EBSD orientation maps. The following SEM and EBSD detector settings were used during EBSD data acquisition: 70° sample tilt; 20 keV accelerating voltage; 150 – 300 magnification (multiple EBSD maps were collected); 14 - 15 mm working distance; 60 µm aperture size; 0.14 µm EBSD step size; and 4×4 data binning.
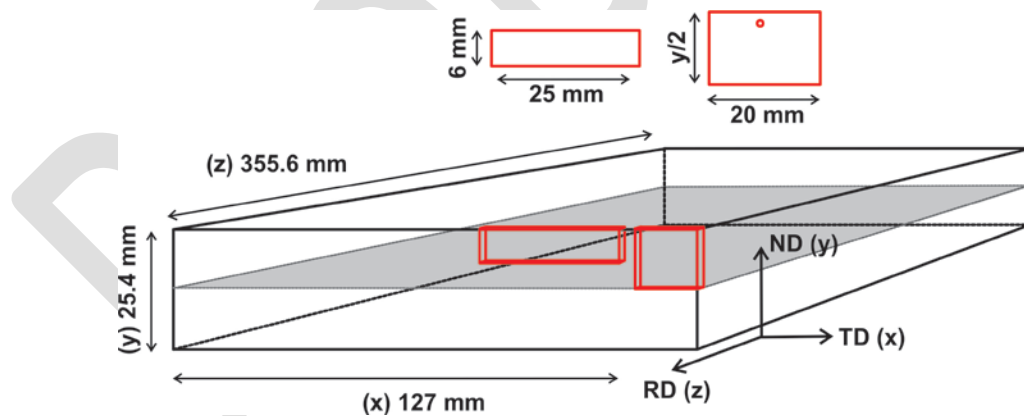

Fig. 1 Schematic drawing of unrolled (0%) plate and the samples for electrochemistry, static corrosion and neutron diffraction measurements. All corrosion samples are 2 mm in thickness, after EDM cutting. ND = Normal Direction; TD = Transverse Direction; and RD = Rolling Direction.

EBSD orientation maps were analyzed using Matlab [30] features in the MTEX toolbox [31, 32]. First, post-processing (filtering) of the raw EBSD orientation data was performed. During this process, all measurement points with the Mean Angular Deviation (MAD) above 0.8 degrees or Band Contrast

6

(BC) below 0.1 were discarded from subsequent data analysis. In the EBSD analysis, a number of standard microstructural characteristics were calculated: (i) Kernel Average Misorientation (KAM), (ii) density of Geometrically Necessary Dislocations (ρ_{GND}) [33], (iii) number of grains [32], and (iv) grain boundary length per unit area.

2.2.2. High-Resolution Neutron Diffraction (HRND)

Full diffraction patterns of the as-received unrolled (0%) and cold-rolled (20%, 30%) SS316L alloys were collected using the ECHIDNA High-Resolution Neutron Diffractometer (HRND) [34]. Samples (5 mm in dimeter and y/2 in height, see Fig. 1) were fully submerged in the neutron beam and continuously rotated during 12 h diffraction pattern acquisition. The resolution of experimental set-up of the instrument was determined using the measurement of standard NIST LaB_6 powder. In order to determine the microstrain ($\langle \varepsilon^2 \rangle$) caused by the presence of dislocations, full diffraction peak broadening (microstrain) analysis was conducted using the GSAS-II software package [35]. Total dislocation density (ρ_T) was then estimated from the measured microstrain ($\langle \varepsilon^2 \rangle$) using the dislocation density model [36]:

$$\rho_T = \frac{k \langle \varepsilon^2 \rangle}{F b^2} \tag{1}$$

where, F is the dislocation interaction factor, k is a constant and b is the magnitude of Burger's vector. For SS316L alloy with FCC crystal lattice and Burger's vector along $\langle 110 \rangle$ direction, $b = 2.5423$ Å, $k = 16.1$, and $F = 1$. F equals 1 is the simplest assumption, which assumes that the interaction between dislocations is negligible.

2.2.3. Volta potential measurements

Scanning Kelvin Probe Force Microscopy (SKPFM) was used for the mapping of Volta potential values of grain and in-grain crystals on the polished surfaces of selected samples. 100 μm^2 rectangular areas (20×5 μm) on the surfaces of an unrolled (0%) and a 30% cold-rolled sample were scanned at a constant rate of 0.4 Hz.

A commercial Atomic Force Microscope (AFM), MFP-3D from Asylum Research, was used for concurrent topography and Volta potential measurement (two-pass technique) from the samples

7

surfaces at room temperature ($\simeq$ 22 ˚C). A single conductive Pt coated probe (NSG03 from NT-MDT) having a nominal resonant frequency of 47-150 kHz was used. In the absence of any z-offset, the probe tip retraced 30 nm above the substrate during the second pass. The Kelvin voltage was maintained with an integral gain of 4 V, no proportional gain, and an AC-voltage of 3 V applied to the tip.

2.3. Corrosion resistance

2.3.1.   Static corrosion measurements

A mixture of eutectic (wt.%) 32.1 Li_2CO_3 + 34.5 K_2CO_3 + 33.4 Na_2CO_3 (melting point = 397 °C; density = 0.77 g.cm^{-3}; thermal conductivity (at 405 °C) $\approx$ 0.6 W.(mK)$^{-1}$) [27, 37] was used in the present study. Test temperature was 450 ˚C, which is close to the salt melting point. This is a suitable operation temperature for TES systems, which can take advantage of latent heat released during the phase change of the salt and is near the temperature of many conventional steam turbines [8, 20, 27, 38, 39]. Five double side-polished SS316L samples of each condition (0%, 20%, and 30% cold-rolled) were immersed in the molten salt. Thicknesses of the samples were recorded (average of 8 - 10 measurements per sample) using a Mitutoyo digital micrometer with the resolution and measurement accuracy of $\pm$ 1 µm. The samples were then submerged in the molten salt, in alumina crucibles, in a preheated furnace at 450 °C open to air and removed after 1000 h. Samples were cooled in air and then submerged in hot water for 10 - 15 minutes for the salt residues to be removed. All samples were found to be covered with a tenacious layer of black corrosion products on all sides.

One sample from each sample set was used for the identification of corrosion products on the sample surface using SEM imaging and Energy Dispersive Spectroscopy (EDS) analysis. These samples were cross-sectioned, mounted in a conductive resin and then polished.

The other four samples from each sample set were cross-sectioned and mounted into a transparent resin exposing the cross-section and polished. To measure the thickness of the metal left after molten salt exposure, excluding corrosion product residues on the surface, an optical microscope model Leica DMi8M was utilized. The micrometer and optical microscope were checked against each other to ensure they both showed the same number when measuring thickness.

To reveal the microstructure and carbide precipitates, mirror-like (as-polished) metallographic samples were also etched in 10 ml glycerin + 6 ml HCl + 3 ml HNO₃ solution [40], before and after molten salt exposure.

2.3.2. Micro-hardness measurements

A micro-Vickers hardness tester, model Matsuzawa MXT70 with 20 s dwell time and 1000 g load, was used to measure micro-hardness values on the samples' cross-sections, before and after exposure to the molten salt. Ten measurement points per sample were recorded with the spacing of >5 times of the indentation diameter between adjacent points, to avoid work hardening. Measurements were done on a straight line in the middle of the samples' thicknesses, which had been ground and polished several millimeters away from the initial surface. Therefore, the micro-hardness data points reflect the hardness values of the bulk material.

2.3.3. Electrochemical measurements

A three-electrode cell, containing the molten carbonate salt mixture (in alumina crucibles) open to the air, was used to conduct electrochemical measurements in a cylindrical furnace preheated to 450 °C using a VMP3-based BioLogic potentiostat controlled by EC-Lab® software. Double-side polished test samples (0%, 20% and 30% cold-rolled, Fig. 1) were subjected to Open Circuit Potential (OCP), Electrochemical Impedance Spectroscopy (EIS) and Linear Polarization Resistance (LPR) measurements. Two platinum sheets (30 × 5 × 1 mm) were used during the experiment – the first platinum sheet was used as a pseudo reference electrode [41, 42] and the second one as a counter electrode. Equilibration of potential (OCP) was carried out for 30 minutes immediately after immersion into the molten salt followed by EIS and LPR. EIS measurements were obtained in the frequency range between 200 kHz and 100 mHz with the amplitude of ± 10 mV. LPR was carried out at the potential scan rate of 10 mV/min and potential range of ± 25 mV with respect to OCP. LPR plots were then analyzed using the polarization resistance (RP) fit tool of EC-Lab® software to calculate R_p, corrosion current density (i_{corr}) and corrosion potential (E_{corr}) values within ± 10 mV from the corrosion potential.

2.3.4. X-ray Photoelectron Spectroscopy (XPS)

X-ray Photoelectron Spectroscopy (XPS) was conducted using monochromatic Al k-alpha radiation on an Axis Supra (Kratos Analytical Ltd) instrument running at a power of 225 Watts. The instrument work function was calibrated to give a Binding Energy (BE) of 83.96 eV for the 4f 7/2 core level of gold, and the spectrometer dispersion was adjusted to give a BE of 932.62 eV for the 2p 3/2 core level of copper. The pass energy was set to 160 eV for survey spectra and 20 eV for high resolution spectra, and all measurements were acquired in a hybrid lens mode which covers an analysis area of 210000 μm^2 (700×300 μm). Spectra were charge corrected to the main line of the carbon 1s core level spectrum set to 284.8 eV.

3. Results

3.1. Effect of cold-rolling on the microstructure of SS316L

Fig. 2 shows the comparison of EBSD orientation maps, in inverse pole figure (IPF) coloring (a-c) and KAM (d-f), of 0%, 20% and 30% cold-rolled samples, respectively. δ-ferrite is shown in white in order to better visualize its presence in the form of long stringers.
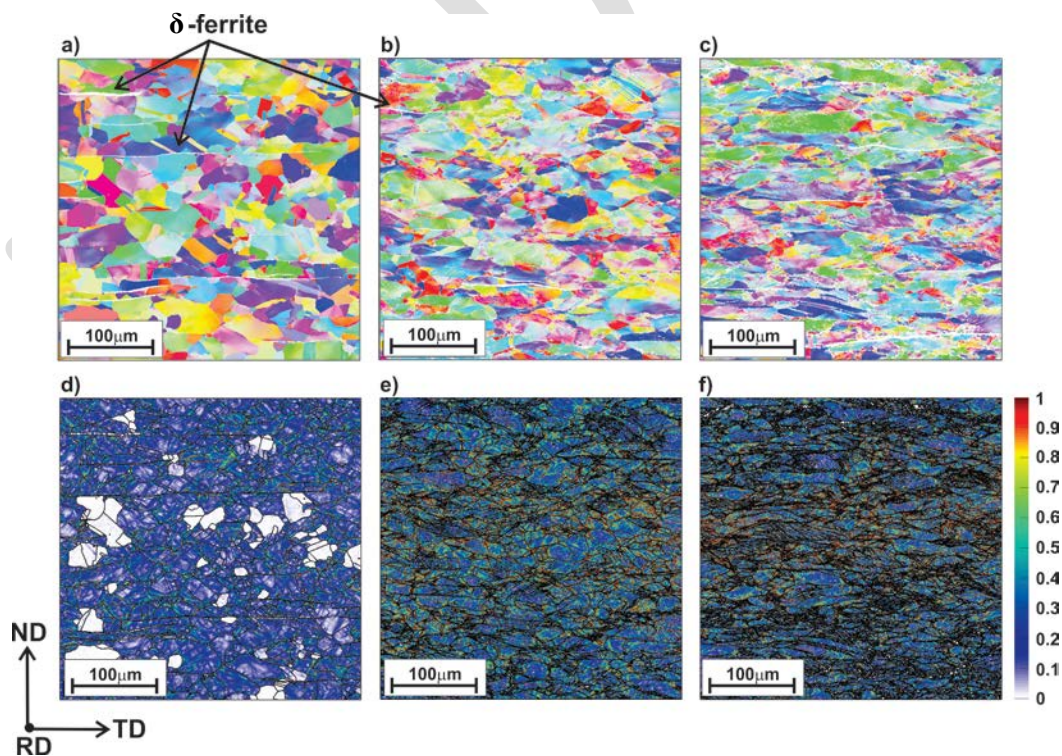

Fig. 2 (a-c) EBSD orientation maps (inverse pole figure color), and (d-f) corresponding KAM analysis maps for samples with 0%, 20% and 30% of cold-rolling (left to right, respectively).

Fig. 3 shows the number of grains per unit area and grain boundary length per unit area as a function of the amount of cold-rolling. These characteristics were calculated from multiple (up to 12) EBSD orientation maps obtained at different locations across the microstructure. It is apparent that the number of detected grains per unit area dramatically increases from about 20k in unrolled (0%) sample to about 720k in 30% cold-rolled sample, respectively. Note that the misorientation angle of 5° (MTEX toolbox [31, 32]) was used in the EBSD analysis to detect grain boundaries. Impact of cold-rolling on the microstructure is even more apparent from the measurement of grain boundary length, which increases from about 0.35 m/mm^2 in unrolled (0%) sample to 2.3 m/mm^2 in 30% cold-rolled sample, respectively. This significant increase is due to the formation of High-Angle Grain Boundaries (HAGBs) during the cold-rolling process because of the accumulation of dislocations and occurrence of deformation twinning. HAGBs have been previously shown to be more susceptible to SCC [43], hence their presence will significantly alter the corrosion behavior of the SS316L alloy.
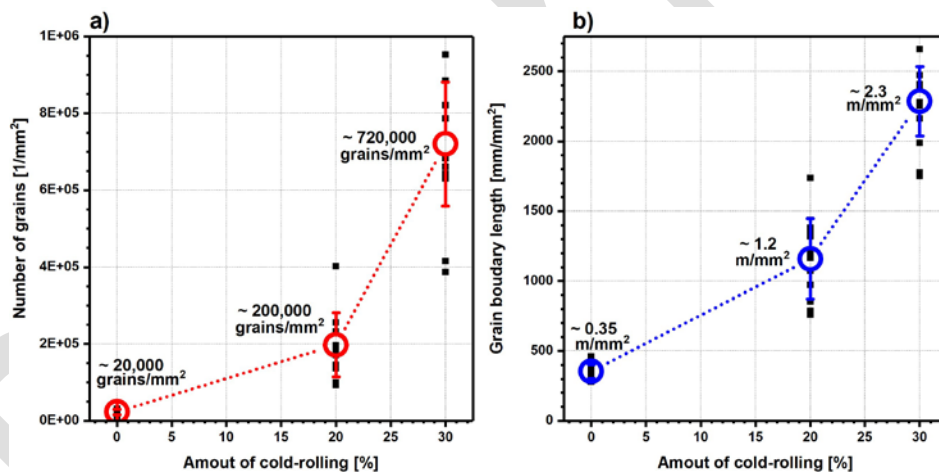

Fig. 3 (a) Mean measured number of grains per unit area, and (b) mean measured grain boundary length per unit area as a function of the amount of cold-rolling for samples with 0%, 20% and 30% of cold-rolling.

Fig. 2 (d-f) shows the KAM maps, which is related to the distribution of Geometrically-Necessary Dislocations (GNDs) across the microstructure. It is clear that GNDs are unevenly distributed in the microstructure forming a network of high and low-angle grain boundaries.

Fig. 4 shows the mean (bulk) KAM and density of GNDs (ρ_{GND}) values obtained by averaging results from multiple EBSD maps thus averaging hundreds of grains (small black symbols show mean KAM and mean density of GNDs (ρ_{GND}) obtained by analysis of individual EBSD maps). It is clear

11

from Fig. 4, and the extracted data summarized in Table 3, that ρ_{GND} increases with the amount of cold-rolling leading to the observed increase in strength and reduction in elongation (see Table 2). Fig. 4b compares the total[*] dislocation density ($\rho_T = \rho_{GND} + \rho_{SSD}$) obtained by the analysis of HRND patterns using GSAS-II (see section 2.2.2) and the ρ_{GND} estimated from the EBSD measurements [33]. It is also clear from Fig. 4b that Statistically-Stored Dislocations (SSDs) represent a significantly higher portion of the present dislocations. Hence, hardening of the studied alloy is largely controlled by the presence of SSDs; also see hardness measurement in Fig. 10.
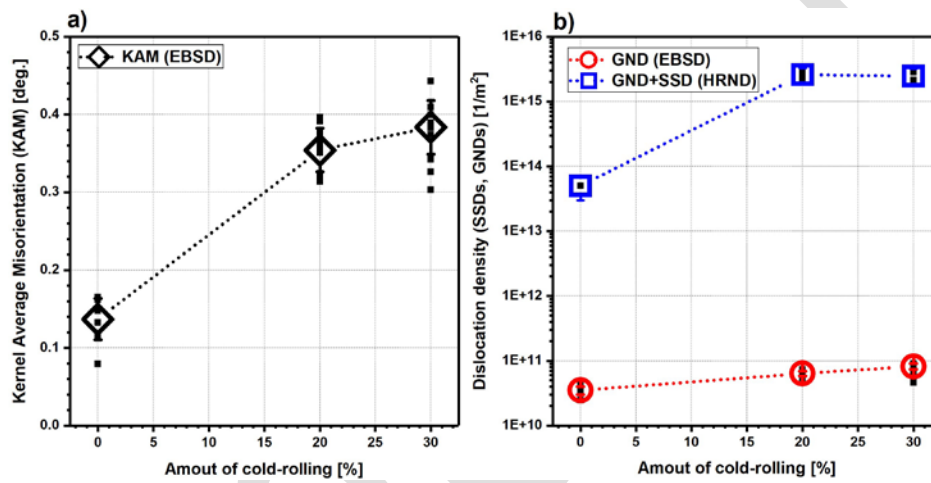

Fig. 4 (a) Mean KAM (calculated by EBSD), and (b) mean dislocation density of GNDs (estimated from EBSD orientation maps) together with mean total (SSDs+GNDs) dislocation density (ρ_T) estimated from peak broadening in HRND pattern.

Table 3 Mean Kernel Angular Misorientation (KAM), and density of GNDs (ρ_{GND}) obtained by the analysis (MTEX) of multiple EBSD maps, and total dislocation density (ρ_T) obtained by the peak-profile (microstrain) analysis (GSAS-II) of HRND patterns.

Sample	KAM (EBSD) [deg.]	ρ_{GND} (EBSD) [1/m^2]	ρ_T (HRND) [1/m^2]
0%	0.14 ($\pm$0.03)	3.5E10 ($\pm$5E09)	5E13 ($\pm$2E13)
20%	0.35 ($\pm$0.03)	6.4E10 ($\pm$5E09)	2.58E15 ($\pm$2E14)
30%	0.38 ($\pm$0.04)	8.2E10 ($\pm$8E09)	2.48E15 ($\pm$2E14)

---

[*] Total dislocation density is the sum of GNDs and Statistically-Stored Dislocations (SSDs). Material hardening is controlled by the both types of dislocations.

3.2. Effect of cold-rolling on the corrosion behavior of SS316L

3.2.1. Volta potential analysis

Fig. 5 shows Volta potential analysis of as-polished mirror-like surfaces of 0% and 30% cold-rolled samples; conducted on fresh samples prior to exposure to elevated temperatures or the molten salt. Note that the measured Volta potential values here are used to compare individual samples' surfaces [20].
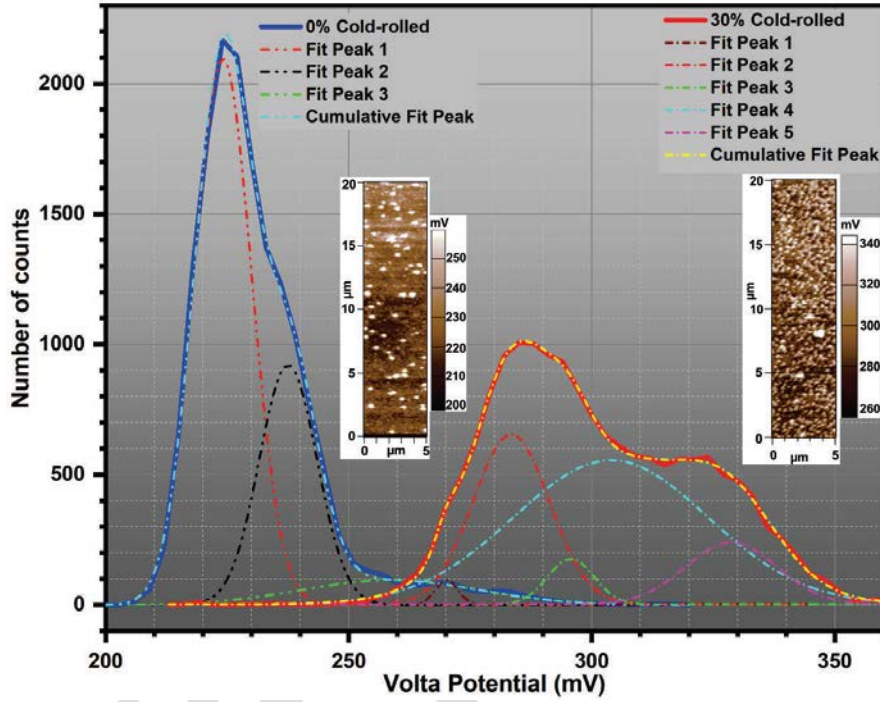

Fig. 5 SKPFM map analyses of 0% and 30% cold-rolled specimens with associated histogram analyses of Volta potential data plus simulated multimodal normal distribution (Gaussian) plots corresponding to each histogram.

For the analytical interpretation of Volta potential values, histogram plots with multimodal Gaussian (normal) distributions of the corresponding spectra were extracted from the SKPFM images. Eq. 2 represents the normal distribution (Gaussian) function used to fit the curves with multiple peaks:

$$y = y_0 + \frac{A}{w\sqrt{\pi/2}} \exp[-\frac{2(x-\mu)^2}{w^2}] \qquad (2)$$

with, $w = 2\sigma$ \hfill (3)

where, y is the counts number, y_0 and A are constant values, x is the Volta potential value, μ refers to the mean value parameter, σ is the standard deviation and w is approximately 0.849 that is the width of the peak at half height. To find the quantity of multimodal distribution peaks, which indicates the

13

number of surface constituents (events probability) [44, 45], the first derivatives of the histograms were calculated together with their inflection points, see Table 4.

The number of multimodal distribution peaks, corresponding mean values (μ) and standard deviations (σ), are generally used to quantitatively evaluate the data acquired [45]. As Fig. 5 indicates, surface heterogeneity resembles a penta-modal distribution for the 30% cold-rolled sample compared to a tri-modal for the unrolled (0%) sample. Note that the shift in the position of the two histograms in Fig. 5 does not point to a significant discrepancy between the two metal samples; since the surface driving force for corrosion attack is indicated only by the difference between the measured Volta potential values, not the absolute values [45].

Table 4 Multimodal normal distribution (Gaussian) parameters extracted from the histograms in Fig. 5.

Sample	Number of modals	Mean value (μ) [mV]	Standard deviation (σ) [mV]	Driving force ($\Delta\mu=\mu_i-\mu_j$) [mV]
0%	3	$\mu_1 = 224$	$\sigma_1 = 6$	35
		$\mu_2 = 238$	$\sigma_2 = 6$	21
		$\mu_3 = 259$	$\sigma_3 = 18$	14
30%	5	$\mu_1 = 270$	$\sigma_1 = 2$	59
				46
		$\mu_2 = 283$	$\sigma_2 = 8$	34
				33
		$\mu_3 = 296$	$\sigma_3 = 5$	26
				25
		$\mu_4 = 304$	$\sigma_4 = 20$	21
				13
		$\mu_5 = 329$	$\sigma_5 = 9$	13
				8

The five peaks detected for the 30% cold-rolled sample, compared with three peaks for the unrolled (0%) sample, indicate a different surface. This shows that the surface of the unrolled (0%) sample is more homogenous compared to the 30% cold-rolled sample with at least five different potential

spans/peaks (different constituents) which are proposed to be texture, the deformed lattice, void defects, dislocations and twinning areas (or a combination of them) at the surface. This is consistent with previous HRND and EBSD observations and confirms the increased surface heterogeneity of the sample with an increase in cold-rolling and subsequent microstructural heterogeneities.

The existence of a greater number of different constituents on the surface of the 30% cold-rolled sample could then lead to the formation of micro-anodic sites (galvanic cells) on the metal surface. Therefore, the cold-rolled sample(s) would be far more at risk of localized attack compared to the unrolled sample. A maximum driving force of 35 mV for the unrolled (0%) sample (Table 4) is to be compared with 59 mV for the 30% cold-rolled sample with a more heterogenized structure.

3.2.2. Electrochemical analysis

To examine the electrochemical interaction of the material with the molten salt, polished mirror-like coupons were used. OCP plots of the test samples, measured for 30 min immediately after immersion in the molten salt, are shown in Fig. 6a. All samples gain nobler potential values over time, which suggest the development of a passive layer on the samples' surfaces. The unrolled (0%) sample stabilizes at potential values around -310 mV after 30 min in the molten salt; compared to -447 and -457 mV for the 20% and 30% cold-rolled samples, respectively. E_{corr} values in LPR plots shown in Fig. 6b reflect OCP values in Fig. 6a with Table 5 summarizing the extracted data values, employing the RP fit tool of the EC-Lab® software. Results confirm the increased susceptibility to corrosion for cold-rolled samples.

Polarization resistance (R_p) is defined as the slope of potential vs. current density curve, Fig. 6c, at the free corrosion potential according to Faraday's law [23, 46]:

$$R_p = (\frac{dE}{di})_{E_{corr}} \tag{4}$$

where, E is the corrosion potential and i is the corrosion current density. Extracted data from the LPR curves of the samples in the molten salt, Table 5, reflect the highest R_p value measured for the unrolled (0%) sample. Accordingly, R_P drops by around 47% and 61% when cold-rolled to 20% and 30% reduction in the thickness, respectively.
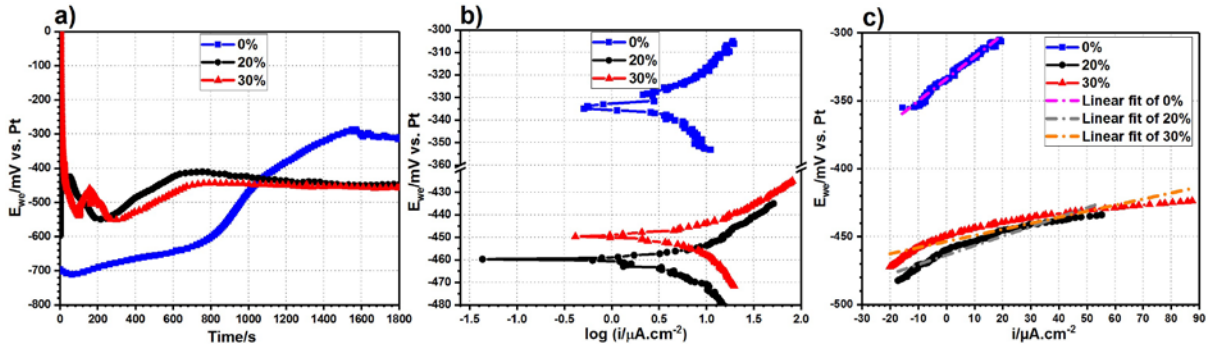
15

Fig. 6 (a) Open Circuit Potential (OCP), (b) E vs. log i curves, and (c) polarization resistance (E vs. i) curves with R_p fit applied for the studied SS316L samples in molten eutectic Li_2CO_3 + K_2CO_3 + Na_2CO_3 at 450 ˚C.

The simultaneous drop of R_P with the reduction of E_{corr} indicates a faster corrosion (oxidation of metal) due to plastic deformation. This is clear from i_{corr} values in Table 5 and the corresponding corrosion rate (*CR*) values, estimated according to [46, 47]:

$$CR = K.EW.\frac{i_{corr}}{\rho} \qquad (5)$$

where, $K = 3.272$ µm.g.µA^{-1}.cm^{-1}.yr^{-1}, *EW* is equivalent weight (= 25.5 for SS316 [46]) and ρ is density (= 7.87 for iron) in g.cm^{-3}.

Table 5 Data extracted from the curves in Fig. 6 and static corrosion data in Fig. 9.

Sample	E_{corr} [mV vs. Pt]	i_{corr} [µA.cm^{-2}]	R_p [Ω.cm^2]	CR [µm/year] Eq. 5	CR [µm/year] Static test
0%	-333	16	1645	170	176
20%	-461	30	873	318	185
30%	-450	41	644	435	196

For further analysis, EIS was measured immediately after OCP. Plots shown in Fig. 7a confirm the development of a double layer capacitive loop in the impedance spectra which accounts for a charge transfer reaction at the steel/melt interface [48]. Considering the OCP data, this confirms the formation of a passive layer on the surface of the metal samples in the molten carbonate salt. The difference between the diameters of semicircles implies a greater charge transfer (polarization) resistance at the surface of the unrolled (0%) sample compared to the 20% and 30% cold-rolled samples [44]. This is also obvious in Bode-phase plots in Fig. 7b and is in good agreement with LPR results. It is noteworthy

16

that the jump/drop seen in the Nyquist plot of 0% sample in Fig. 7a is probably due to a noise from the electrical grid.
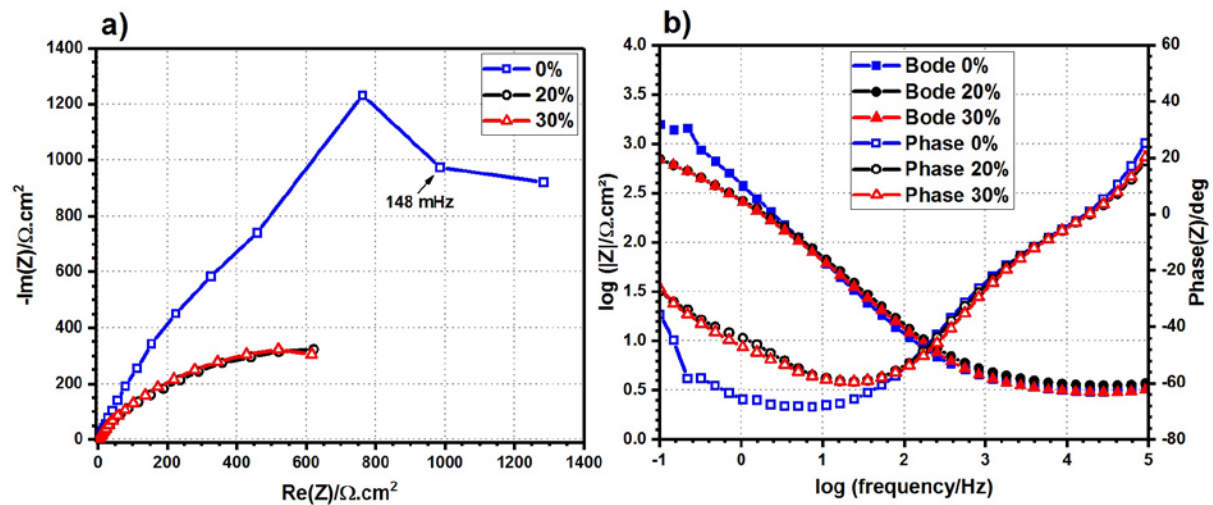

Fig. 7 (a) Nyquist and (b) Bode-phase curves measured using EIS tests of the studied samples in molten eutectic $Li_2CO_3 + K_2CO_3 + Na_2CO_3$ at 450 ˚C.

3.2.3. Static corrosion

To investigate the salt impact on SS316L over longer times, one sample of each set was examined by SEM-EDS analysis after 1000 h exposure to the molten eutectic carbonate salt at 450 ˚C. SEM-EDS results for a 30% cold-rolled sample are shown in Fig. 8. Clearly seen is the presence of a Fe-depleted and oxidized (O-rich) layer close to the metal surface. The penetration depth of this de-alloyed oxide zone is between 1.5 and 3.3 µm. Grain boundary de-alloying and oxidation is observed towards the bulk material. A tenacious and continuous layer of iron-chromium oxide (Fe-Cr-O) is also detectable on the sample surface with a thickness of around 1.9 µm.

The rest of the post-immersion samples (four from each set) were examined under a light microscope (5× magnification) to measure thickness reduction after 1000 h exposure to the molten eutectic carbonate salt. At least 6 measurements per sample were taken and average values recorded. The average thickness of each sample, average thickness of each set (mean values) and deviation from standard values (σ) are shown in Fig. 9. The unrolled (0%) sample set show an average of 176 µm/year reduction in metal thickness. There is a 5% and 11% increase of this reduction value for 20% cold-rolled set (185 µm/year) and 30% set (196 µm/year), respectively (Table 5). It is evident that the slight

17

increase in corrosion rate corresponds to the previous trend observed via LPR and reduction of R_P values with the related increase in the amount of cold-rolling.
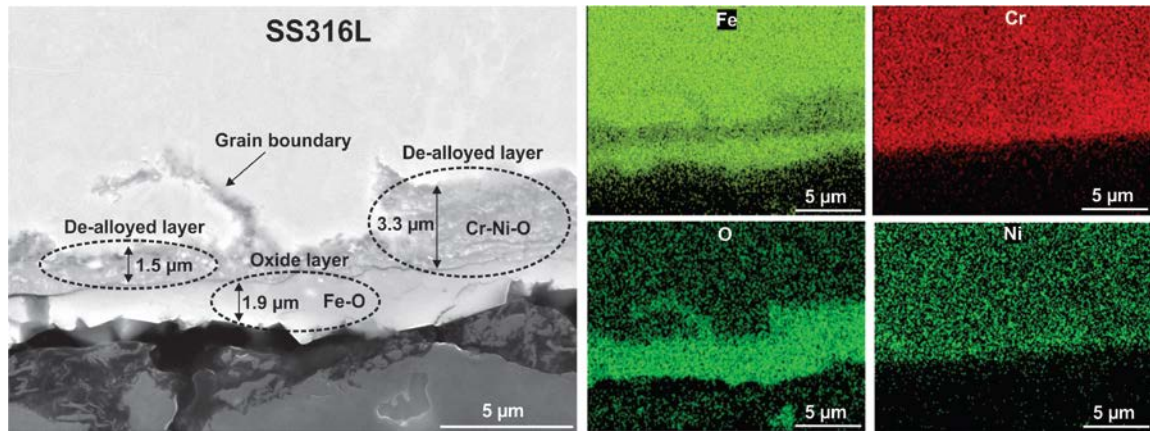

Fig. 8 Cross-section SEM image and its corresponding EDS map analysis of a 30% cold-rolled sample after 1000 h exposure to the molten eutectic carbonate salt at 450 ˚C.

One sample from each set was selected for micro-hardness measurement. Fig. 10 compares micro-hardness for each set of samples before and after 1000 h exposure to the molten salt at 450 ˚C. A negligible reduction from the initial state is seen for the unrolled (0%) set. However, both the 20% and 30% cold-rolled sets get noticeably harder. This was not expected since the samples should have been stress-relieved and the microstructure recovered after being exposed to the hot temperature for such a long time.
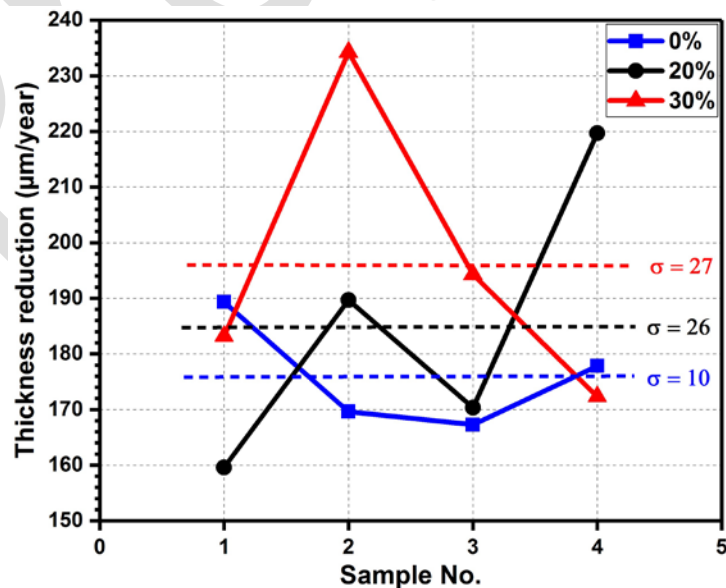

Fig. 9 Thickness reduction after 1000 h exposure to the molten eutectic carbonate salt at 450 ˚C; dash lines show average values and σ is deviation from the mean value.
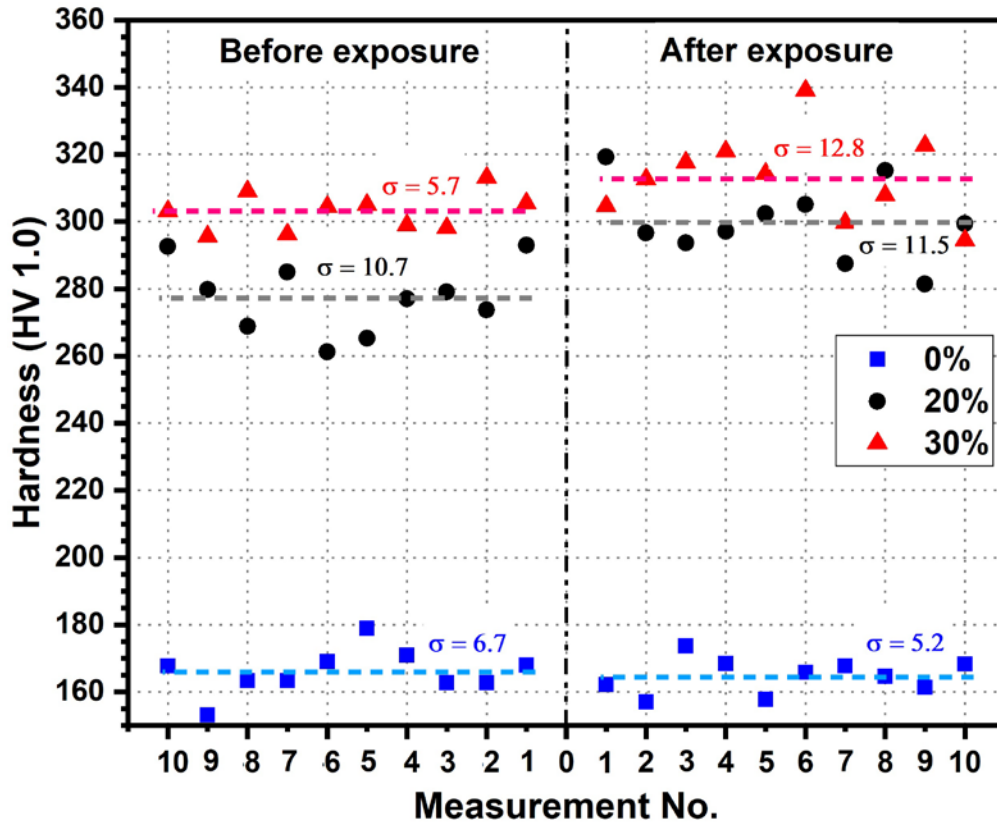
Fig. 10 Hardness profiles of the samples in as-received condition (left) and after 1000 h exposure to the molten eutectic carbonate salt at 450 ˚C (right); dash lines show average values and σ is deviation from the mean value.

To determine why the observed increase in micro-hardness occurred, samples were etched in a 10 ml glycerin + 6 ml HCl + 3 ml HNO_3 solution (as discussed in section 2.3.1) and the microstructure was observed under light microscope and SEM. Fig. 11 compares and contrasts the microstructure of a 20% cold-rolled sample, before and after exposure. Furthermore, SEM images of a 30% cold-rolled sample prior to exposure, tilted 70˚ for better observation, is shown in Fig. 12. Microstructure before exposure consists of δ-ferrite in an austenitic texture with protruded nodular chromium carbides [40, 49-51] mostly distributed along grain boundaries (GBs) and slip planes. However, the carbide nodules have disappeared after 1000 h exposure to the molten salt at 450 ˚C, Fig. 11d.

EDS point analyses of spectrums in Fig. 11c and d are provided in Table 6. A significant increase in the carbon content of the alloy is seen after exposure. This indicates carburization has occurred because of exposure to the molten eutectic carbonate salt for 1000 h at 450 ˚C.
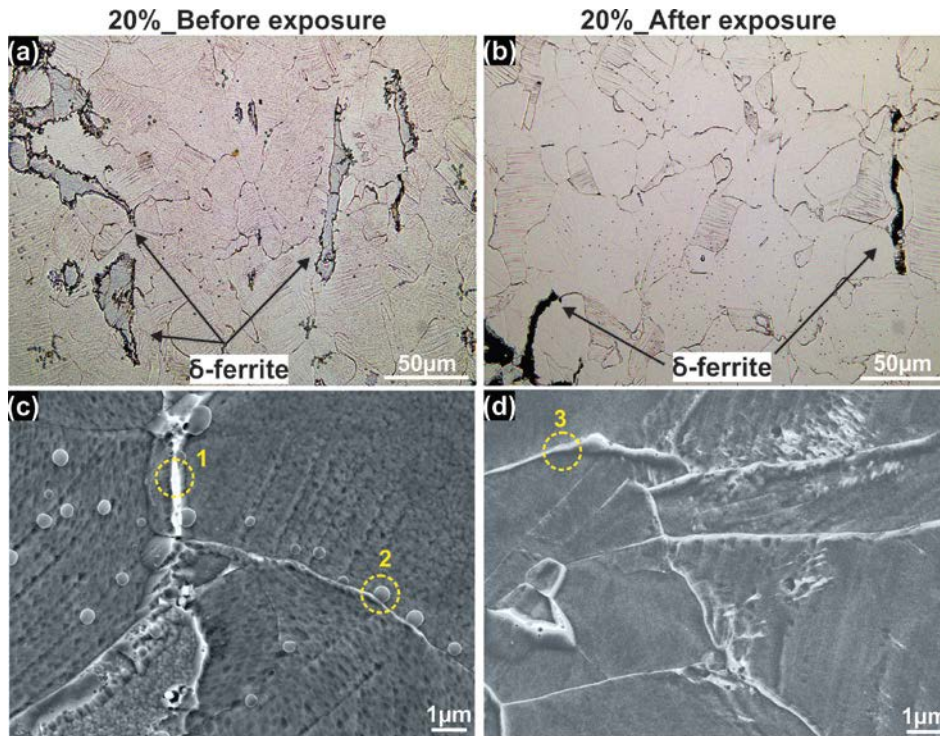
19

Fig. 11 (a, c) Optical and SEM images of an as-received 20% cold-rolled sample, (b, d) optical and SEM images of a 20% cold-rolled sample after 1000 h exposure to the molten eutectic carbonate salt at 450 ˚C.

Carbon concentration was also measured by XPS for a post-corrosion 30% cold-rolled sample; as-polished cross-section of the same sample that was used for bulk micro-hardness measurement. A 5 keV Ar$^+$ ion source was used for sample cleaning and depth profiling. Fig. 13 shows carbon concentration for 9 measurements with high resolution C spectra for the last two surveys, i.e. surveys 8 and 9. Results confirm the material consists of around 6 at.% (or 1 wt.%) C in the composition (average of surveys 4 to 9). This is around 50 times higher than its initial concentration of about 0.02 wt.%, see Table 1. The inset in Fig. 13 shows the peak position of carbon to be around 283 eV which is a characteristic of carbidic C. This confirms that C is in solid-solution on the interstitial sites of the γ-austenitic matrix [52].

Table 6 EDS point analyses (chemical composition in wt.%) of grain boundaries and nodular carbides in Fig. 11

(c and d) for 20% cold-rolled samples before and after exposure to the molten salt.

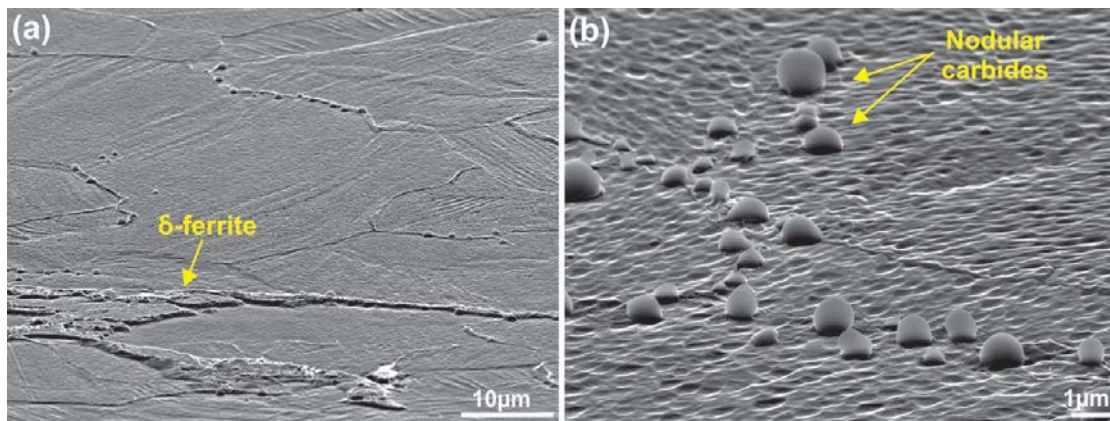| Element	Fe	C	Cr	Ni	Others
Point 1 (GB before exposure)	59.3	12.6	17.7	5.4	Bal.
Point 2 (nodular carbide)	57.5	17.6	14.3	8.2	Bal.
Point 3 (GB after exposure)	45.3	34.9	11.5	5.8	Bal.

Fig. 12 SEM micrographs of an as-received 30% cold-rolled sample (70˚ titled) showing protruded nodular
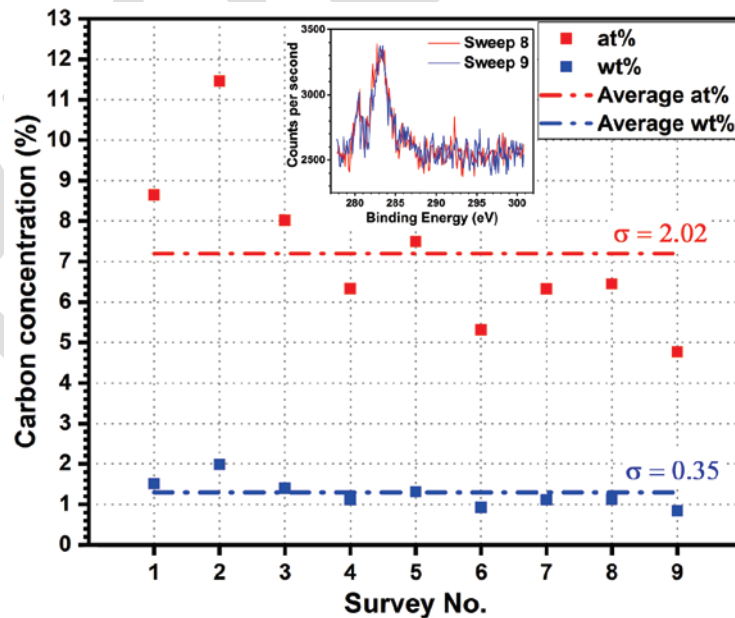
carbide precipitates along grain boundaries.

Fig. 13 Depth profile measurement of carbon by XPS with high resolution C spectra for a 30% cold-rolled

sample after 1000 h exposure to the molten carbonate salt at 450 ˚C.

4. Discussion

The dramatic increase in the number of grains and length of HAGBs per unit area (Fig. 3) due to cold-rolling is accompanied with a significant increase in the density of dislocations (GNDs, SSDs) as shown in Fig. 4b. According to Raabe [25], increased lattice defects such as HAGBs and dislocations is associated with an increase in the internal energy of the material. The presence of dislocations on the surface of a cold-rolled material leads to potential alteration in their vicinity. Consequently, the thermodynamic stability of the material reduces according to Gibbs free energy theorem [25, 53, 54]. This is evident from Volta potential measurements in Fig. 5 suggesting the development of micro-galvanic cells on the sample surface because of the heterogeneous distribution of dislocations across the microstructure, see Fig. 2 and Table 4.

The distribution of stored energy has already been reported to significantly affect the material behavior in service [25]. The R_P drop shown in Table 5 results from the increased charge transfer rate of the material in cold-rolled condition because of the higher amounts of internal energy stored in the material. This causes an increase in the driving force for localized attack and subsequently faster corrosion rates due to plastic deformation which destabilizes the cold-rolled material in the first few hours of exposure.

Corrosion mechanisms of steel alloys (and nickel alloys) in molten carbonate salts have been discussed in detail [4, 20]. Considering the ionic nature of liquid salts, their interaction with metals is electrochemical and therefore metal oxidation reflects the partial anodic reaction [55, 56]:

$$M \rightarrow M^{n+} + ne^- \tag{6}$$

$$2M^{n+} + nO^{2-} \rightarrow 2MO_n \tag{7}$$

where, M is the transition metal such as Fe, Cr and Ni. Reduction of oxygen as the partial cathodic reaction follows [55]:

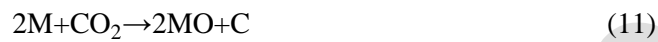$$Ox + ne^- \rightarrow R \tag{8}$$

where, n points to the number of electrons, and Ox and R refer to oxidant and reductant, respectively. Previous studies maintain that, in molten salts, corrosion depends on the solubility of the formed metal oxides on the material surface [4, 5, 57]. Liquid N_2CO_3 carbonates- where N stands for alkali metals

such as Li, Na or K- can dissociate to their basic and acidic components; N_2O and CO_2, respectively [58]. Then, according to Eq. 9, the high oxygen reduction rate (which results from the very high solubility of oxygen in the liquid salt) causes the basic component to dissociate into the melt [55, 58]:

$$N_2O \leftrightarrow 2N^+ + O^{2-} \qquad\qquad (9)$$

Finally, the reduction of highly reactive oxide ions (O^{2-}) on the metal surface oxidizes the metal [55, 59]. Production of CO_2, on the other hand, can carburize the austenitic steel according to the reactions [11, 60]:

$$M + CO_2 \rightarrow MO + CO \qquad\qquad (10)$$

$$2M + CO_2 \rightarrow 2MO + C \qquad\qquad (11)$$

$$M + CO \rightarrow MO + C \qquad\qquad (12)$$

Despite of the formation of an oxide layer on the metal surface (as shown in Fig. 8), which has been already reported to cease the above reactions [60], the observed hardening of the cold-rolled material after 1000 h exposure (see Fig. 10) is a clear evidence of the substrate metal not being effectively protected by the oxide layer formed on its exposed surface. This could be because of carbon diffusion through this layer to the bulk material. Carburization here is facilitated by the presence of the introduced lattice defects such as dislocations, void defects and grain boundaries because of plastic deformation.

This could also be referred to as interstitial hardening of the steel by low temperature carburization which has been previously reported by Niu et al. [61] when SS316L is exposed to a $CO-CO_2$ gas mixture at 470 ˚C. The term *low temperature* here could be defined as a temperature which is low enough to kinetically suppress carbide precipitation, but still high enough to enable interstitial carbon diffusion into the bulk material [52, 61, 62]. As well as hardening, Cao et al. [52, 62, 63] reported a general increased resistance to corrosion because of the super-saturation of austenite with up to 12 at.% carbon as long as it stays in solid solution. The absence of lattice defects, on the other hand, prevented the unrolled (0%) sample from bulk-material carburization.

The corrosion rate estimated for the unrolled (0%) sample calculated with electrochemistry theory concurs with that from the gravimetric method (Table 5). The difference between corrosion rates

23

reported from electrochemical measurement and static corrosion data for the cold-rolled samples, however, could be an indication of ongoing recovery due to the exposure of the material to high temperature for a long time [20, 25]. During the first few hours of exposure, the corrosion rate is higher due to the presence of a large number of dislocations and material instability as discussed above. As an accelerated test, it is also expected that electrochemical measurements will show different corrosion rates compared to gravimetric methods (especially at long exposure times), since potential sweeps affect corrosion layers formed on the material surface [7, 64]. Therefore, the corrosion rate is relatively high (318 and 435 µm/year) for cold-rolled samples during the first few hours as measured by electrochemistry (Table 5). Then, metal stabilization due to recovery and the subsequent establishment of an oxide layer on the surface (as shown in Fig. 8) could lead to reduced corrosion rates (185 and 196 µm/year) at longer times for cold-rolled samples (Table 5). Carburization could be another reason for the reduced corrosion rate of cold-rolled samples after longer exposure times, as discussed above. Fast corrosion at the first few hours of exposure for the cold-rolled samples could therefore account for the slight increase in the corrosion rate after 1000 h.

Conclusion

Electrochemical, microstructural, hardness, Kelvin probe force and neutron diffraction investigations were utilized to investigate the impact of plastic deformation (cold-rolling) on the interaction of SS316L with molten eutectic Li_2CO_3 + K_2CO_3 + Na_2CO_3 at 450 ˚C for thermal energy storage applications.

High-Resolution Neutron Diffraction in conjunction with Electron Back-Scatter Diffraction showed a dramatic increase in the number of grains, grain boundaries and density of dislocations because of imparted plastic deformation during the cold-rolling process. The presence of these crystal lattice defects causes reduction in the thermodynamic stability of the alloy, which leads to the formation of micro-galvanic cells on the sample surface as shown by Volta potential measurements.

Increased driving force for localized corrosion attack, due to the development of micro-galvanic cells, was observed according to reduction in the polarization resistance of the alloy in contact with the molten carbonate salt at 450 °C leading to accelerated corrosion because of cold-rolling during the first

24

few hours of exposure. However, material stabilization (probably due to recovery) and development of an oxide layer on the surface were found to decelerate corrosion at longer times of exposure (up to 1000 h). Cold-rolling was also found to facilitate carburization and subsequent material hardening because of carbon diffusion from the molten carbonate salt through the introduced lattice defects at long exposure times (1000 h). XPS analysis confirmed a carbon concentration of about 1 wt.% in cold-rolled samples. Solid solution of carbon in austenite contributed to further resistance against corrosion. No evidence of bulk material carburization was found on the unrolled samples.

Acknowledgement

References

[1] G.Q. Zheng, B. Kelleher, G.P. Cao, M. Anderson, T. Allen, K. Sridharan, Corrosion of 316 stainless steel in high temperature molten Li2BeF4 (FLiBe) salt, Journal of Nuclear Materials, 461 (2015) 143-150.

[2] K. Sridharan, T.R. Allen, 12 - Corrosion in Molten Salts, in: F.L. Groult (Ed.) Molten Salts Chemistry, Elsevier, Oxford, 2013, pp. 241-267.

[3] M. Maric, O. Muránsky, I. Karatchevtseva, T. Ungár, J. Hester, A. Studer, N. Scales, G. Ribárik, S. Primig, M.R. Hill, The effect of cold-rolling on the microstructure and corrosion behaviour of 316L alloy in FLiNaK molten salt, Corrosion Science, 142 (2018) 133-144.

[4] M. Sarvghad, T.A. Steinberg, G. Will, Corrosion of steel alloys in eutectic NaCl+Na 2 CO 3 at 700 °C and Li 2 CO 3 + K 2 CO 3 + Na 2 CO 3 at 450 °C for thermal energy storage, Solar Energy Materials and Solar Cells, 170 (2017) 48-59.

[5] M. Sarvghad, G. Will, T.A. Steinberg, Corrosion of steel alloys in molten NaCl + Na 2 SO 4 at 700 °C for thermal energy storage, Solar Energy Materials and Solar Cells, 179 (2018) 207-216.

[6] F. Subari, H.F. Maksom, A. Zawawi, Corrosion Behavior of Eutectic Molten Salt solution on Stainless Steel 316L, Procedia - Social and Behavioral Sciences, 195 (2015) 2699-2708.

[7] M. Walczak, F. Pineda, Á.G. Fernández, C. Mata-Torres, R.A. Escobar, Materials corrosion for thermal energy storage systems in concentrated solar power plants, Renew Sust Energ Rev, 86 (2018) 22-44.

[8] M. Liu, W. Saman, F. Bruno, Review on storage materials and thermal performance enhancement techniques for high temperature phase change thermal storage systems, Renew Sust Energ Rev, 16 (2012) 2118-2132.

[9] S. Riahi, Y. Jovet, W.Y. Saman, M. Belusko, F. Bruno, Sensible and latent heat energy storage systems for concentrated solar power plants, exergy efficiency comparison, Solar Energy, 180 (2019) 104-115.

[10] Á.G. Fernández, M. Fullana, L. Calabrese, E. Proverbio, L.F. Cabeza, Corrosion Characterization in Components for Thermal Energy Storage Applications, in: A. Frazzica, L.F. Cabeza (Eds.) Recent Advancements in Materials and Systems for Thermal Energy Storage, Springer International Publishin, 2019, pp. 139-169.

[11] M. Sarvghad, S.D. Maher, D. Collard, M. Tassan, G. Will, T.A. Steinberg, Materials compatibility for the next generation of Concentrated Solar Power plants, Energy Storage Materials, 14 (2018) 179-198.

[12] R.K. Desu, H. Nitin Krishnamurthy, A. Balu, A.K. Gupta, S.K. Singh, Mechanical properties of Austenitic Stainless Steel 304L and 316L at elevated temperatures, Journal of Materials Research and Technology, 5 (2016) 13-20.

[13] P. Yvon, F. Carré, Structural materials challenges for advanced reactor systems, Journal of Nuclear Materials, 385 (2009) 217-222.

[14] M. Milad, N. Zreiba, F. Elhalouani, C. Baradai, The effect of cold work on structure and properties of AISI 304 stainless steel, Journal of Materials Processing Technology, 203 (2008) 80-85.

[15] A. Kelly, K.M. Knowles, Dislocations, in: Crystallography and Crystal Defects, John Wiley & Sons Ltd, 2012, pp. 241-267.

[16] A. Kelly, K.M. Knowles, Point Defects, in: Crystallography and Crystal Defects, John Wiley & Sons Ltd, 2012, pp. 305-334.

[17] A. Kelly, K.M. Knowles, Twinning, in: Crystallography and Crystal Defects, John Wiley & Sons Ltd, 2012, pp. 335-361.

[18] M. Calcagnotto, D. Ponge, E. Demir, D. Raabe, Orientation gradients and geometrically necessary dislocations in ultrafine grained dual-phase steels studied by 2D and 3D EBSD, Materials Science and Engineering: A, 527 (2010) 2738-2746.

[19] M.C. Rezende, L.S. Araújo, S.B. Gabriel, J. Dille, L.H. de Almeida, Oxidation assisted intergranular cracking under loading at dynamic strain aging temperatures in Inconel 718 superalloy, J Alloy Compd, 643 (2015) S256-S259.

[20] M. Sarvghad, T. Chenu, G. Will, Comparative interaction of cold-worked versus annealed inconel 601 with molten carbonate salt at 450°C, Corrosion Science, 116 (2017) 88-97.

[21] G. Ilevbare, A.R. McIlree, E.P.R. Institute, A.E.o.C. Limited, C.O. Group, Program on Technology Innovation: Proceedings : 2007 AECL/COG/EPRI Workshop on Cold Work in Iron- and Nickel-Base Alloys Exposed to High Temperature Water Environments : June 3-8, 2007, Mississauga, Ontario, Electric Power Research Institute, 2008.

[22] P.L. Andresen, C.L. Briant, Environmentally Assisted Cracking of Types 304L/316L/316NG Stainless Steel in 288°C Water, Corrosion, 45 (1989) 448-463.

[23] S. Lyon, Overview of corrosion engineering, science and technology, in: Nuclear Corrosion Science and Engineering, Elsevier Ltd, 2012, pp. 3-30.

[24] N. Ishiyama, M. Mayuzumi, Y. Mizutani, J.-i. Tani, Stress Corrosion Cracking of Type 316 and 316L Stainless Steel in High Temperature Water, in: T.R. Allen, P.J. King, L. Nelson (Eds.) Environmental Degradation of Materials in Nuclear Power System – Water Reactors, TMS (The Minerals, Metals & Materials Society), 2005.

26

[25] D. Raabe, Recovery and Recrystallization: Phenomena, Physics, Models, Simulation, in: D.E.L. Hono (Ed.) Physical Metallurgy (Fifth Edition), Elsevier, Oxford, 2014, pp. 2291-2397.

[26] B.C. Shin, S.D. Kim, W.-H. Park, Ternary carbonate eutectic (lithium, sodium and potassium carbonates) for latent heat storage medium, Solar Energy Materials, 21 (1990) 81-90.

[27] R. Raud, R. Jacob, F. Bruno, G. Will, T.A. Steinberg, A critical review of eutectic salt property prediction for latent heat energy storage systems, Renew Sust Energ Rev, 70 (2017) 936-944.

[28] R.I. Olivares, C. Chen, S. Wright, The Thermal Stability of Molten Lithium–Sodium–Potassium Carbonate and the Influence of Additives on the Melting Point, Journal of Solar Energy Engineering, 134 (2012) 041002-041002.

[29] M.M. Nowell, R.A. Witt, B. True, EBSD Sample Preparation: Techniques, Tips, and Tricks, Microscopy and Microanalysis, 11 (2005).

[30] MATLAB, MATLAB 2015, in, 2015.

[31] R. Hielscher, MTEX 3.5.0, in, 2015.

[32] F. Bachmann, R. Hielscher, H. Schaeben, Grain detection from 2d and 3d EBSD data--specification of the MTEX algorithm, Ultramicroscopy, 111 (2011) 1720-1733.

[33] W. Pantleon, Resolving the geometrically necessary dislocation content by conventional electron backscattering diffraction, Scripta Materialia, 58 (2008) 994-997.

[34] K.-D. Liss, B. Hunter, M. Hagen, T. Noakes, S. Kennedy, Echidna—the new high-resolution powder diffractometer being built at OPAL, Physica B: Condensed Matter, 385-386 (2006) 1010-1012.

[35] B.H. Toby, R.B. Von Dreele, GSAS-II: the genesis of a modern open-source all purpose crystallography software package, Journal of Applied Crystallography, 46 (2013) 544-549.

[36] G.K. Williamson, R.E. Smallman, III. Dislocation densities in some annealed and cold-worked metals from measurements on the X-ray debye-scherrer spectrum, Philosophical Magazine, 1 (1956) 34-46.

[37] R. Raud, Optimized salt selection for solar thermal latent heat energy storage, in: Science & Engineering Faculty, Queensland University of Technology, 2018.

[38] E. González-Roubaud, D. Pérez-Osorio, C. Prieto, Review of commercial thermal energy storage in concentrated solar power plants: Steam vs. molten salts, Renew Sust Energ Rev, 80 (2017) 133-148.

[39] M. Liu, N.H.S. Tay, S. Bell, M. Belusko, R. Jacob, G. Will, W. Saman, F. Bruno, Review on concentrating solar power plants and new developments in high temperature thermal energy storage technologies, Renewable & Sustainable Energy Reviews, 53 (2016) 1411-1432.

[40] R.I. Olivares, D.J. Young, P. Marvig, W. Stein, Alloys SS316 and Hastelloy-C276 in Supercritical CO2 at High Temperature, Oxidation of Metals, 84 (2015) 585-606.

[41] A.I. Bhatt, G.A. Snook, Reference Electrodes for Ionic Liquids and Molten Salts, in: G. Inzelt, A. Lewenstam, F. Scholz (Eds.) Handbook of Reference Electrodes, Springer Berlin Heidelberg, 2013, pp. 189-227.

[42] G. Inzelt, Pseudo-reference Electrodes, in: G. Inzelt, A. Lewenstam, F. Scholz (Eds.) Handbook of Reference Electrodes, Springer Berlin Heidelberg, 2013, pp. 331-332.

[43] S.P. Lynch, 1 - Mechanistic and fractographic aspects of stress-corrosion cracking (SCC), in: V.S. Raja, T. Shoji (Eds.) Stress Corrosion Cracking, Woodhead Publishing, 2011, pp. 3-89.

[44] A. Davoodi, Z. Esfahani, M. Sarvghad, Microstructure and corrosion characterization of the interfacial region in dissimilar friction stir welded AA5083 to AA7023, Corrosion Science, 107 (2016) 133-144.

[45] M. Sarvghad-Moghaddam, R. Parvizi, A. Davoodi, M. Haddad-Sabzevar, A. Imani, Establishing a correlation between interfacial microstructures and corrosion initiation sites in Al/Cu joints by SEM–EDS and AFM–SKPFM, Corrosion Science, 79 (2014) 148-158.

[46] ASTM G102-89(2015)e1, in: Standard practice for calculation of corrosion rates and related information from electrochemical measurements, ASTM International, West Conshohocken, PA, 2015.

[47] K. Vignarooban, P. Pugazhendhi, C. Tucker, D. Gervasio, A.M. Kannan, Corrosion resistance of Hastelloys in molten metal-chloride heat-transfer fluids for concentrating solar power applications, Solar Energy, 103 (2014) 62-69.

27

[48] C.L. Zeng, W. Wang, W.T. Wu, Electrochemical impedance models for molten salt corrosion, Corrosion Science, 43 (2001) 787-801.

[49] C. Sudha, N. Sivai Bharasi, R. Anand, H. Shaikh, R.K. Dayal, M. Vijayalakshmi, Carburization behavior of AISI 316LN austenitic stainless steel – Experimental studies and modeling, Journal of Nuclear Materials, 402 (2010) 186-195.

[50] S.R. Pillai, N.S. Barasi, H.S. Khatak, A.L.E. Terrance, R.D. Kale, M. Rajan, K.K. Rajah, Corrosion behavior and tensile properties of AISI 316LN stainless steel exposed to flowing sodium at 823 K, Journal of Materials Engineering and Performance, 9 (2000) 98-102.

[51] N. Sivai Bharasi, K. Thyagarajan, H. Shaikh, A.K. Balamurugan, S. Bera, S. Kalavathy, K. Gurumurthy, A.K. Tyagi, R.K. Dayal, K.K. Rajan, H.S. Khatak, Effect of flowing sodium on corrosion and tensile properties of AISI type 316LN stainless steel at 823K, Journal of Nuclear Materials, 377 (2008) 378-384.

[52] Y. Cao, F. Ernst, G.M. Michal, Colossal carbon supersaturation in austenitic stainless steels carburized at low temperature, Acta Materialia, 51 (2003) 4171-4181.

[53] G. Gottstein, L.S. Shvindlerman, Grain boundary migration in metals: thermodynamics, kinetics, applications, 2 ed., CRC press, 2009.

[54] L.S. Shvindlerman, G. Gottstein, Cornerstones of grain structure evolution and stability: Vacancies, boundaries, triple junctions, Journal of Materials Science, 40 (2005) 819-839.

[55] A. Nishikata, H. Numata, T. Tsuru, Electrochemistry of molten salt corrosion, Materials Science and Engineering: A, 146 (1991) 15-31.

[56] S.N. Liu, Z.D. Liu, Y.T. Wang, J. Tang, A comparative study on the high temperature corrosion of TP347H stainless steel, C22 alloy and laser-cladding C22 coating in molten chloride salts, Corrosion Science, 83 (2014) 396-408.

[57] M. Sarvghad, G. Will, T.A. Steinberg, Corrosion of Inconel 601 in molten salts for thermal energy storage, Solar Energy Materials and Solar Cells, 172 (2017) 220-229.

[58] M.L. Orfield, D.A. Shores, Solubility of NiO in Molten Li_2CO_3, Na_2CO_3, K_2CO_3, and Rb_2CO_3 at 910°C, J Electrochem Soc, 135 (1988) 1662-1668.

[59] A. Nishikata, S. Haruyama, Electrochemical Studies of the Corrosion of Ni and Fe in Molten Carbonate, J Jpn I Met, 48 (1984) 720-725.

[60] R. Moore, T. Conboy, Metal Corrosion in a Supercritical Carbon Dioxide - Liquid Sodium Power Cycle, in, Sandia National Laboratories, Albuquerque, New Mexico,. Livermore, California, 2012.

[61] W. Niu, R.S. Lillard, Z. Li, F. Ernst, Properties of the Passive Film Formed on Interstitially Hardened AISI 316L Stainless Steel, Electrochim Acta, 176 (2015) 410-419.

[62] F. Ernst, Y. Cao, G.M. Michal, A.H. Heuer, Carbide precipitation in austenitic stainless steel carburized at low temperature, Acta Materialia, 55 (2007) 1895-1906.

[63] G. Michal, F. Ernst, H. Kahn, Y. Cao, F. Oba, N. Agarwal, A. Heuer, Carbon supersaturation due to paraequilibrium carburization: Stainless steels with greatly improved mechanical properties, Acta Materialia, 54 (2006) 1597-1606.

[64] B. Zhu, G. Lindbergh, D. Simonsson, Comparison of electrochemical and surface characterisation methods for investigation of corrosion of bipolar plate materials in molten carbonate fuel cell Part II. Surface analysis, Corrosion Science, 41 (1999) 1515-1528.